Transport in Porous Media **50:** 179–195, 2003.

Transition to Chaos and Flow Dynamics of Thermochemical Porous Medium Convection

STAN SCHOOFS[1] and FRANK J. SPERA[2]
[1]*GeoDelft, Strategic Research Department, Stieltjesweg 2, Delft, The Netherlands*
[2]*Department of Geological Sciences and Institute for Crustal Studies, University of California, Santa Barbara, CA 93106, U.S.A.*

(Received: 13 March 2001; in final form: 9 October 2001)

Abstract. In a fluid-saturated porous medium, dissolved species advect at the pore velocity, while thermal retardation causes heat to move at the Darcy velocity. The Darcy model with the Boussinesq approximation in a square medium with a porosity of $\phi = 0.01$ subject to two sources of buoyancy is used, to study numerically the dynamics of this so-called double-advective instability. The vertical walls of the medium are impermeable and adiabatic, while Dirichlet boundary conditions are imposed on the horizontal walls such that the medium is heated and salted from below. For an increasing ratio between chemical and thermal buoyancy, while keeping the thermal buoyancy fixed, a transition from a steady to a chaotic convective solution is observed. At the transition a stable limit cycle is found, suggesting that the transition takes the form of a Hopf bifurcation. The dynamics of the chaotic flow is characterized by irregular transitions between nonlayered and layered flow patterns, as a result of the spontaneous formation and disappearance of gravitationally stable interfaces. These interfaces temporarily divide the domain in layers of distinct solute concentration and lead to a significant reduction of kinetic energy and vertical heat and solute fluxes. The stability of an interface is described by a balance between the viscous drag forces in the convective layers and the buoyancy force associated with the density interface.

Key words: free convection, chaos, coupled flow, structure formation, force balance.

1. Introduction

Convection of fluid in a saturated porous medium has been studied intensively during the past few decades. Most of the work, both mathematically and experimentally, has been devoted to the conditions for the onset of motion and the flow dynamics of convection driven by temperature differences alone (see Nield and Bejan, 1999 for a review).

In most natural circumstances, however, the fluid is subject to more than one source of buoyancy. Thermochemical convection (TCC) is a fluid dynamical phenomenon in which two sources of buoyancy, heat and solute, drive the flow. TCC of purely viscous fluids is well known in the context of oceanography (Schmitt, 1995) and is characterized by the different diffusive behavior of heat and solute.

Like of purely viscous fluids, the dynamics of TCC in porous media is fundamentally different from flow driven by the temperature field only. TCC of fluids

in porous media deviates also from TCC of purely viscous fluids in the sense that the difference in heat and solute transport is rather double-advective than double-diffusive: the dissolved species advect at the pore velocity q/ϕ, while thermal retardation causes heat to move at the Darcy velocity q (Phillips, 1991). The occurrence of the double-advective instability becomes apparent especially in media of low porosity, like are vast amounts of the Earth's continental and oceanic crust (Fisher, 1998; Manning and Ingebritsen, 1999). TCC, therefore, has implications for many geological processes, such as crustal heat and solute transport, metamorphism, the diagenetic evolution of sedimentary basins and ore genesis (Person *et al.*, 1996; Oldenburg and Pruess, 1998). Besides its importance in the hydrogeological context, thermochemical convection in porous media has a wide variety of (geo)technical applications, among them contaminant transport in saturated soil, underground disposal of nuclear wastes, liquid re-injection (Oldenburg and Pruess, 1999), the migration of moisture in fibrous insulation, and electro-chemical and drying processes.

In this study, the double-advective instability is studied by means of numerical simulations of flow in a two-dimensional square domain with a porosity of $\phi = 0.01$. The medium is heated and salted from below, in order to resemble roughly the hydrogeological situation in the Earth's upper crust. Focus is on the form of the transition from steady to chaotic convection, which is observed when the ratio of chemical over thermal buoyancy increases while the thermal buoyancy is held constant. Furthermore, the flow dynamics in the chaotic regime is investigated, by performing a detailed analysis of the convection simulations performed by Schoofs *et al.* (1999).

First, the governing equations and the employed numerical method are described (§2). In Section 3, a concise literature review is given. The flow dynamics of TCC at low porosity is described in Section 4. In Section 5, the transition from the steady convective regime to the chaotic regime is studied, by analyzing the numerical data of simulations with various buoyancy ratios and spatial resolutions. In Section 6, focus is on the transitions between layered and nonlayered flow patterns, as commonly observed in the chaotic regime. The stability of a density interface between two convective layers is described in terms of a force balance. The paper ends with a discussion of the results (§7).

2. Formulation and Numerical Method

An incompressible fluid in a rigid, homogeneous, and isotropic porous medium is considered, Darcy's law is assumed for conservation of momentum, and the Boussinesq approximation is applied. A standard Fickian model is considered for the mechanical dispersion of the dissolved species (Bear, 1972). Dispersion of heat is neglected. A linearized equation of state ($\rho = \rho_0[1 - \alpha(T - T_0) + \beta(C - C_0)]$) is employed (where ρ [kg/m^3] is fluid density, α [K^{-1}] and β [wt%$^{-1}$] are thermal and chemical expansivity, T [K] is temperature, C [wt%] is chemical concentra-

tion, and reference values are denoted by the subscript 0). The laws for conservation of mass, momentum, energy, species, together with the equation of state describe convection in porous media mathematically (see Schoofs *et al.*, 1999, 2000 for more detailed definitions). The equations were nondimensionalized with the height of the domain h [m] as the length scale, $h^2\sigma/\kappa$ [s] as time scale, $\mu\kappa/K$ [Pa] as dynamic pressure scale, and $\Delta T = T_1 - T_0$ [K] and $\Delta C = C_1 - C_0$ [wt%] as the temperature and salinity scale, respectively (maximum values of T and C are denoted by the subscript 1). Here, σ [$-$] represents the ratio of the heat capacities between the solid matrix and the fluid $\sigma = \phi + (1-\phi)(\rho c_p)_{\text{matrix}}/(\rho c_p)_{\text{fluid}}$, with c_p [J/m^3] the isobaric heat capacity. In this study, $\sigma = 1$.

In non-dimensionless form, the system of equations in a two-dimensional setting is given by

$$\nabla^2 p = \text{Ra}_T \left(R_\rho \frac{\partial C}{\partial z} - \frac{\partial T}{\partial z} \right), \tag{1}$$

$$\frac{\partial T}{\partial t} - \nabla^2 T + \mathbf{q} \cdot \nabla T = 0, \tag{2}$$

$$\begin{aligned} \phi^* \frac{\partial C}{\partial t} + \mathbf{q} \cdot \nabla C \;=\; & \frac{\partial}{\partial x} \left(\left(f_1 + \frac{1}{\text{Le}_{\text{mol}}} \right) \frac{\partial C}{\partial x} + f_3 \frac{\partial C}{\partial z} \right) + \\ & + \frac{\partial}{\partial z} \left(f_3 \frac{\partial C}{\partial x} + \left(f_2 + \frac{1}{\text{Le}_{\text{mol}}} \right) \frac{\partial C}{\partial z} \right), \end{aligned} \tag{3}$$

where

$$f_1 = \frac{a_t(a_r q_x^2 + q_z^2)}{|\mathbf{q}|}, \qquad f_2 = \frac{a_t(a_r q_z^2 + q_x^2)}{|\mathbf{q}|}, \qquad f_3 = \frac{a_t((a_r - 1) q_x q_z)}{|\mathbf{q}|}.$$

Here x [m], z [m] are the Cartesian coordinates, p [Pa] is pressure, t [s] is time, $\mathbf{q}$ [m/s] is Darcy velocity, and a_l [m] and a_t [m] are the longitudinal and transversal dispersivity, respectively.

The six dimensionless parameters governing the convective dynamics are the thermal Rayleigh number Ra_T (a measure of the strength of the heat flow driving the flow), buoyancy ratio R_ρ (the ratio of chemical over thermal buoyancy), effective porosity ϕ^*, longitudinal dispersivity a_t, dispersivity ratio a_r, and the molecular Lewis number, Le_{mol} (ratio between the effective thermal diffusivity of the saturated medium, κ [m^2/s], and the molecular diffusivity of the chemical component within the fluid, D_w [m^2/s], multiplied by the tortuosity of the medium, τ [$-$]). These dimensionless parameters are defined as

$$\text{Ra}_T = \frac{\alpha K \rho_0 g \Delta T h}{\kappa \mu}, \qquad R_\rho = \frac{\beta \Delta C}{\alpha \Delta T},$$

$$\phi^* = \frac{\phi}{\sigma}, \qquad a_r = \frac{a_l}{a_t}, \qquad \text{Le}_{\text{mol}} = \frac{\tau \kappa}{D_{\text{w}}}.$$

Here μ [Pa s] denotes dynamic fluid viscosity, K [m^2] is permeability, g [m/s^2] is gravitation, and ϕ [$-$] is porosity. Scale analysis of (2) and (3) shows that dissolved species advect at the pore velocity $\mathbf{q}/\phi^*$, while temperature advects with the Darcy velocity $\mathbf{q}$. In the following, parameters are dimensionless unless specified otherwise.

Equations (1)–(3) are solved on a cell-centered grid with a second-order finite volume multigrid method. Spatially, a central approximation is used for the diffusive fluxes. The flux-limited Fromm scheme is employed for the advective compositional fluxes to preserve the monotonicity of the solution at sharp interfaces (Hundsdorfer and Trompert, 1994). The non-limited version of this scheme is used for the advective thermal fluxes. Time integration is carried out by an implicit Crank–Nicolson method for the thermal diffusion and an explicit Adams–Bashforth scheme for the advection and the chemical dispersion terms. Validation of the code was accomplished by comparison with published results on thermal convection and TCC (Steen and Aidun, 1988; Rosenberg and Spera, 1992). Further details of the method are given by Schoofs (1999).

Figure 1 displays the configuration of the model together with the boundary conditions. A square domain with impermeable boundaries is considered. The temperature and chemical concentration at the bottom boundary are equal to 1, while at the top both quantities are fixed to zero. In this way heat destabilizes the liquid, while the solute provides a stabilizing influence. The vertical walls are insulators with respect to heat and solute transport. Initially, the motionless fluid is cold and chemically depleted. The fluid is perturbed simply by giving the lower left grid point a temperature $T = 10^{-3}$.

The thermal (chemical) Nusselt number, which is the ratio of the actual heat (solute) flux to the flux that would occur via heat (solute) conduction alone, is

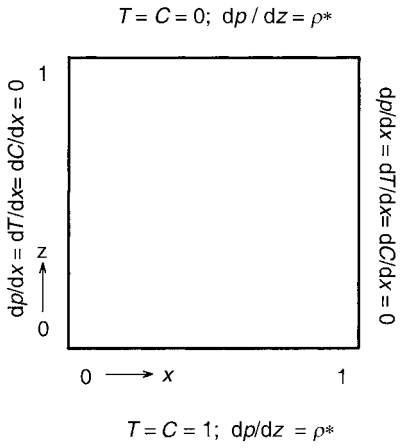

Figure 1. Geometrical setup and boundary conditions of the experiments in a porous medium, which is heated and salted from below. Initially, both temperature T and chemical concentration C are zero.

defined as

$$\mathrm{Nu}_T = -\overline{\frac{\partial T}{\partial z}} \quad \text{at } z = 1 \tag{4}$$

and

$$\mathrm{Nu}_C = -\overline{\left(f_3 \frac{\partial C}{\partial x} + \left(f_2 + \frac{1}{\mathrm{Le}_{\mathrm{mol}}} \right) \frac{\partial C}{\partial z} \right)} \quad \text{at } z = 1, \tag{5}$$

where the overbar implies the horizontal average. The spatially-averaged kinetic energy per unit mass of fluid *KE*, a convenient measure of the vigor of the flow, is defined as

$$KE = \tfrac{1}{2} \langle q_x^2 + q_z^2 \rangle, \tag{6}$$

where the brackets denote the global average.

3. Literature Review of Thermochemical Convection in Porous Media

The onset of TCC in porous media has first been studied by means of linear stability analysis (Nield, 1968). Rudraiah *et al*. (1982) applied nonlinear stability analysis to the case of a porous layer with isothermal and isosolutal boundaries. Numerical and analytical solutions of the flow dynamics of TCC were obtained by Trevisan and Bejan (1987), Rosenberg and Spera (1992), Alavyoon (1993), Alavyoon *et al*. (1994), Mamou *et al*. (1995, 1998), Cooper *et al*. (1997, 2001), and Mamou and Vasseur (1999), for the case of a rectangular medium under various thermal and solutal boundary conditions.

Laboratory experiments at moderate to high Rayleigh numbers have shown, that TCC in porous media takes the form of a boundary layer flow (Griffiths, 1981). Griffiths' experiments also proved that a thin horizontal density interface between two convective layers can be maintained against diffusive thickening. Finally, Griffiths determined heat and solute fluxes of the layered convective system, including a dependence of heat flux on interfacial deflections. Murray and Chen (1989) showed experimentally and numerically that in the presence of a stabilizing salinity gradient, the onset of convection is marked by a dramatic increase in heat flux at a critical temperature difference value. Moreover, the heat flux curve established a hysteresis loop, when the temperature difference is reduced to subcritical values.

On the basis of nonlinear perturbation theory and the parallel flow approximation (valid for shallow or slender enclosures), Mamou and Vasseur (1999) predict analytically the flow behavior of TCC. The results indicate that convection can arise at Rayleigh numbers below the supercritical value in terms of linear stability analysis, indicating the development of subcritical flows. They also showed that multiple solutions exist for a given set of parameters in the overstable regime.

The effect of porosity on the dynamics of TCC has been studied explicitly by Mamou *et al*. (1998) for porosities between 1 and 0.1. By solving the full governing equations these authors showed, that decreasing porosity from $\phi = 0.4$ to

$\phi = 0.1$ leads to a transition from a periodic oscillatory solution to a multi-periodic solution. Other parameters were a moderate thermal Rayleigh number of $\mathrm{Ra}_T = 50$, a buoyancy ratio of $R_\rho = 1$, an aspect ratio of $A = 4$, and a diffusivity ratio of 10. Mechanical dispersion of solute was neglected. The multi-periodic solution evolves towards a convective flow varying from single to multilayered roll cells and vice versa.

The stability and dynamics of double-advective, double-diffusive convection in porous media were studied in Schoofs *et al*. (1999), for the case in which the porous medium is heated from below, while chemical concentration provides a stabilizing influence. The thermal Rayleigh number Ra_T, the buoyancy ratio R_ρ, and the porosity ϕ of the medium were varied systematically. Within the whole set of experiments, the system evolved to one of the following states: (1) static diffusive, (2) steady convective, (3) oscillatory convective, and (4) chaotic convective. The system of equations was integrated numerically until one of the stages could clearly be distinguished. In contrast to the dynamics for an effective porosity of $\phi^* = 0.1$, for which most solutions evolve to the static diffusive state, the dynamics at $\phi^* = 0.01$ appeared to behave almost intrinsically chaotic.

Except the abovementioned studies, studies of the route to chaos have been limited to pure thermal convection in a medium heated from below. By means of solving the full governing equations, Kimura *et al*. (1986, 1989) showed that the transition from steady to chaotic convection occurs through a number of bifurcations to multiple periodic regimes. Vadasz and Olek (1999) and Vadasz (1999) studied the transition to chaos by means of both a truncated Galerkin approximation, which yields a system equivalent to the familiar Lorenz equations, and the Adomian's decomposition method that yields an analytical solution in terms of infinite power series. Vadasz and Olek (1999) showed that the transition is characterized by a stable solitary limit cycle. They concluded that the transition takes the form of a Hopf bifurcation. Vadasz (1999) also reports on a hysteresis at the transition: the critical value of the Rayleigh number is smaller when approaching the transition from the steady convective to the chaotic regime, as compared to the value found in the reverse direction.

4. Dynamics at Low Porosity

It is intuitive for the phenomena studied in this paper (transition to chaos and stability of interfaces) to describe first the flow dynamics in the chaotic regime. Figure 2 shows the thermal and chemical distributions of a simulation at eight stages during the evolution, for parameters $\mathrm{Ra}_T = 600$, $R_\rho = 1$, $a_t = 5 \times 10^{-5}$, $a_r = 10$, $\phi^* = 0.01$, and $\mathrm{Le}_{\mathrm{mol}} = 100$. A dark (light) shading indicates a high (low) temperature or chemical concentration. The spatial numerical resolution used is 64×64 grid cells, based on extensive testing with various spatial and temporal discretizations (see also §5). The grid cells are refined in vertical direction near the base and the top of the domain in order to resolve the horizontal boundary layers. The flow

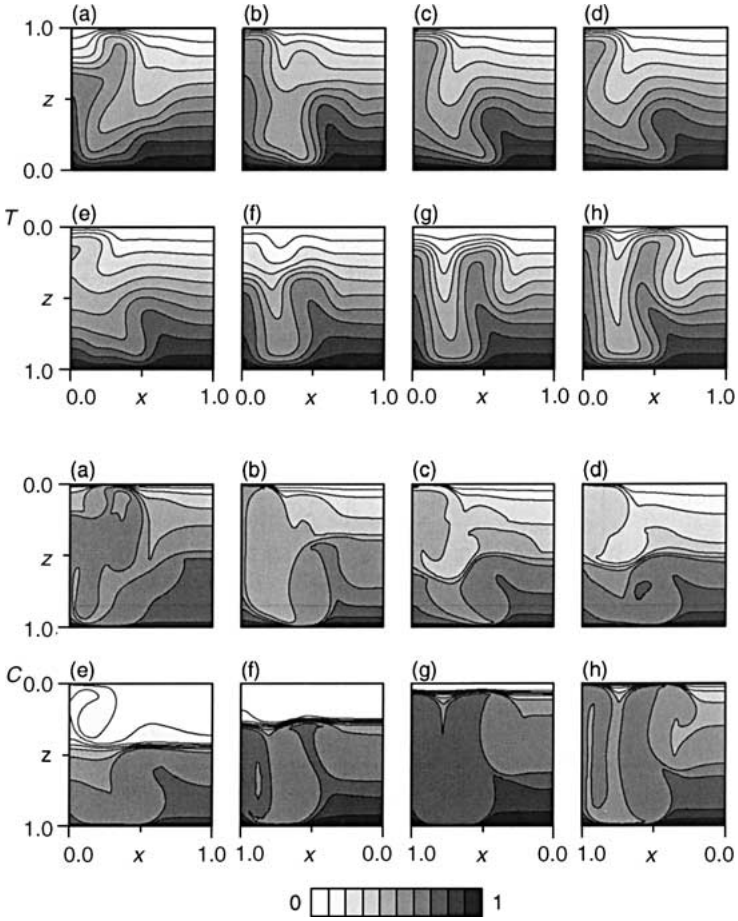

Figure 2. Temperature and salinity snapshots of a flow with parameters $\mathrm{Ra} = 600$, $R_\rho = 1.0$, $\mathrm{Le}_{\mathrm{mol}} = 100$, $\phi^* = 0.01$, $a_t = 5 \times 10^{-4}$, and $a_r = 10$. The corresponding times are (a) $t = 1.2505$, (b) $t = 1.2641$, (c) $t = 1.2692$, (d) $t = 1.2720$, (e) $t = 1.2848$, (f) $t = 1.3034$, (g) $t = 1.3089$, and (h) $t = 1.3105$. Snapshots (a)–(d) show a transition from a single layered to a layered system by the formation of an interface, while snapshots (e)–(f) describe the migration and disappearance of this interface.

appears chaotic during the whole course of the simulation, while it reaches a statistically steady state at $t \approx 0.2$ (for the Nusselt number evolution see Figures 3(c) and (f). The flow is characterized by frequent transitions between nonlayered and layered flow patterns.

A typically nonlayered situation is shown in Figure 2(a). The flow pattern exist of a mixture of advective and (nearly) diffusive areas. The transition from a nonlayered to layered situation is shown in Figures 2(b)–(d). The formation of the interface starts with the development of two thermal instabilities in the upper left and lower right corners (Figure 2(b)). Fast advective mixing of chemical concentration within these regions results in (1) the formation of patches with a

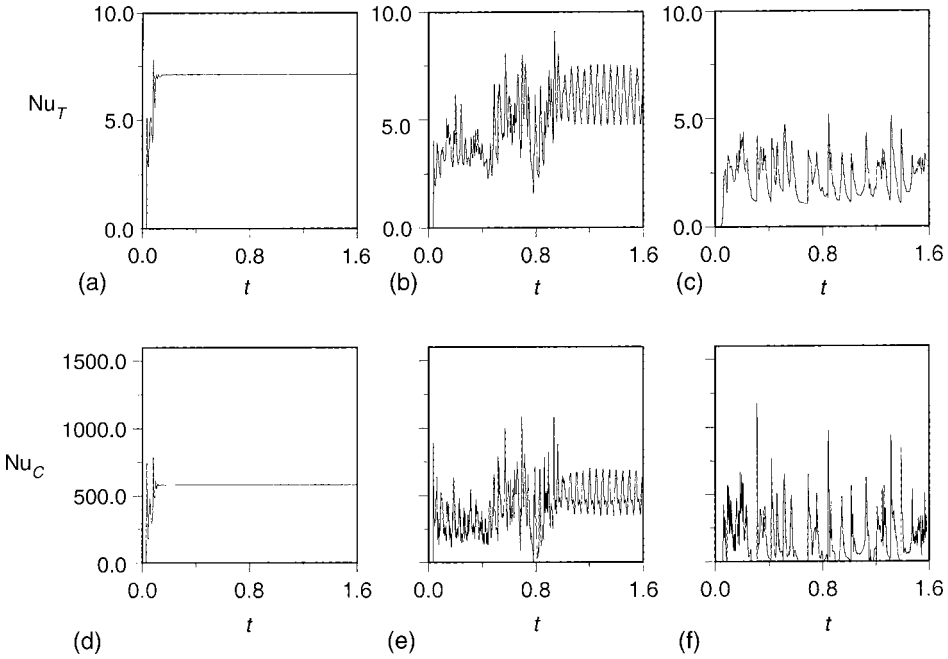

Figure 3. (a)–(c) Temporal evolution of Nu_T and Nu_C for three simulations with (a) $R_\rho = 0.25$, (b) $R_\rho = 0.4$, (c) $R_\rho = 1.0$. Other parameters are $\mathrm{Ra} = 600$, $\mathrm{Le}_{\mathrm{mol}} = 100$, $\phi^* = 0.01$, $a_t = 5 \times 10^{-4}$, and $a_r = 10$ (modified from Schoofs *et al.*, 1999, with permission).

homogenized solute concentration, and (2) the growth of these patches by convective entrainment. At $t = 1.2692$ (Figure 2(c)), a highly distorted interface has developed in between the two areas, that have a different chemical concentration. Further mixing of the separate patches increases the solute (and thus density) difference across the interface. As a result, the distortions of the interface flatten until an almost horizontal interface has evolved (Figure 2(d)).

In Figures 2(e)–(h) the transition from a layered to nonlayered flow pattern is shown. In Figures 2(e)–(g), the interface is visible as the clustering of several horizontal isopleths halfway the domain. The interface divides the domain into two separately convecting layers of another chemical concentration (Figure 2(e)). When the convective vigor in the lower layer increases, fluid is entrained convectively from above the interface into the lower layer. Consequently, the interface migrates gradually upward until it merges with the upper boundary layer (Figures 2(f)–(h)). Both upward and downward moving interfaces were observed. In Section 6, the stability of the density interfaces is analyzed in more detail.

5. Transition to Chaos

In TCC, several routes through the parameter regime lead to the transition from steady to chaotic convection. First, a transition from steady to chaotic convection

through oscillatory flow occurs, by increasing the thermal Rayleigh number and keeping the buoyancy ratio constant (Rosenberg and Spera, 1992). At least for low buoyancy ratios, this transition behaves similarly to the one found in pure thermal convection, the latter studied extensively by Kimura *et al*. (1986, 1989) and Vadasz (1999).

Apart from this transition, a transition to chaos occurs when R_ρ is increased while Ra_T is kept constant. This transition is visible in the evolution of the Nusselt numbers shown in Figure 3, for parameters $\mathrm{Ra}_T = 600$ and $\phi^* = 0.01$ and buoyancy ratios of $R_\rho = 0.25$, $R_\rho = 0.4$, and $R_\rho = 1.0$. For $R_\rho = 0.25$, the system evolves quickly to a steady state (Figures 3(a) and (d)). For $R_\rho = 0.4$, both heat and solute transport become oscillatory after a chaotic initial stage (Figures 3(b) and (e)). The double-periodic flow behavior is due to slightly instable boundary layers at the top and bottom of the domain (Schoofs *et al*., 1999). For $R_\rho = 1.0$, finally, both surface fluxes remain unsteady up to the end of the simulation (Figures 3(c) and (f)). Furthermore, the time-averaged heat flux is reduced considerably as compared to the fluxes at a lower chemical contrast, because part of the internal energy which enters the domain through the bottom is used to transport the denser chemical elements upwards. Finally, heat and solute fluxes are reduced mostly during periods in which an interface exists.

The difference between the convective dynamics for the three buoyancy ratios is further illustrated in the kinetic energy (*KE*) phase plots and power spectra shown in Figure 4. Figure 4(a) shows the *KE* phase plot for $R_\rho = 0.25$. Here, the $KE - \partial KE/\partial t$ trajectory spirals into a stable fixed point. Next, Figure 4(b) shows the *KE* phase plot for the second case, with $R_\rho = 0.4$. The $KE - \partial KE/\partial t$ trajectory follows an irregular orbit in a broader region of phase space, until it becomes an almost perfect limit cycle (see the inset at the right top of the figure for a close-up view of the limit cycle). This suggests that a Hopf bifurcation takes place. Note the different scales at the vertical axes. Furthermore, the average kinetic energy has decreased considerably, as compared to that for $R_\rho = 0.25$ at steady state. Finally, Figure 4(c) displays the *KE* phase plot for $R_\rho = 1.0$. The $KE - \partial KE/\partial t$ trajectory follows an irregular orbit in an even wider loosely defined region and never reaches a fixed point or limit cycle.

Figures 4(d)–(f) show the positive part of the corresponding power spectra of the kinetic energy, for time periods in which the steady, oscillatory or statistically steady states have been evolved completely. For calculation of the power spectra, the averages of the signals have been subtracted and a boxcar window has been used. For $R_\rho = 0.25$, no prevailing frequency is observed (Figure 4(d)). The *KE* power spectrum for the oscillatory state, $R_\rho = 0.4$, contains two dominant frequencies (19 and 41) along with their harmonics (Figure 4(e)). Finally, the *KE* power spectrum for $R_\rho = 1.0$ is depicted in Figure 4(f). In this case, the spectrum is characterized by broadband noise. The most dominant frequencies are between 20 and 25. These frequencies correspond with the development and disappearance of the chemical interfaces.

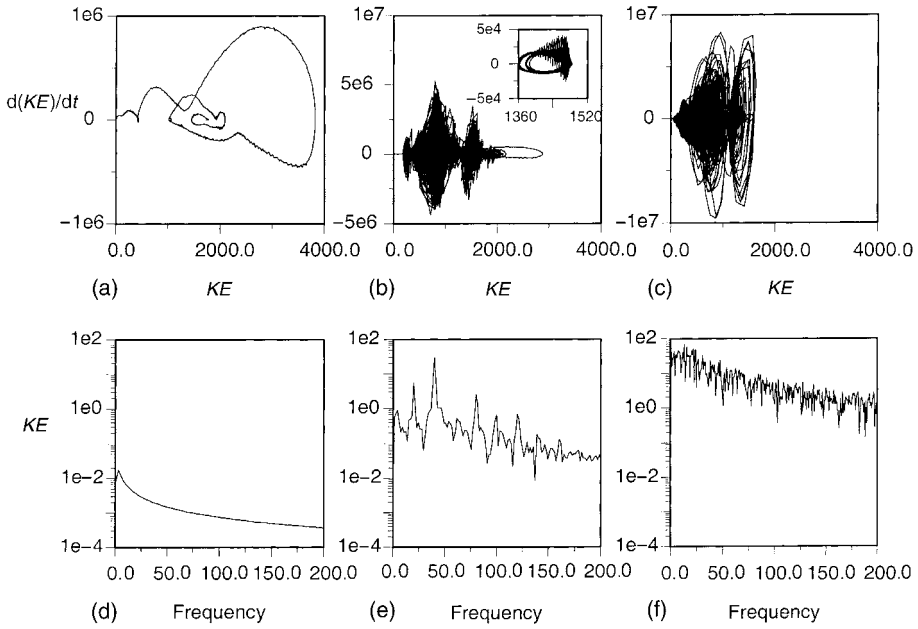

Figure 4. (a)–(c) The KE phase plots showing the trajectory in $KE - \partial KE/\partial t$ space for the three experiments shown in Figures 3. (d)–(f) The accompanying positive parts of the power spectra of the kinetic energy, for periods in which the convection has reached its final evolutionary state. The average is subtracted from the signal.

The influence of the employed spatial resolution on the transition to chaos is shown by plotting the kinetic energy KE for several buoyancy ratios around the critical value on various grids (Figure 5). For decreasing cell size, the transition between steady and chaotic convection shifts to a lower buoyancy ratio: from $R_\rho = 0.5 - 0.6$ on a 32×32 grid, to $R_\rho \approx 0.4$ on a 64×64 grid, to $R_\rho \approx 0.3$ on a 128×128 grid.

6. Stability of a Density Interface

The formation and evolution of separately convecting layers was studied before in detail for effective porosities between $\phi^* = 1.0$ and 0.1 (Schoofs *et al.*, 1998, 2000). In simulations in which an initially linear salinity profile was heated from below, it was shown that growth of a convective layer at the bottom of the domain through convective entrainment, the formation of a stable density interface on top of the layer and destabilization of the next layer are intimately linked. By monitoring the heat (solute) fluxes, it was observed that the transport of heat (solute) across the interface changes from convective entrainment towards a regime in which transfer is purely diffusive (dispersive). The layer growth stops when the density interface on top has grown sufficiently strong to keep the ascending plumes in the lower layer from convectively entraining more fluid from above. A simple

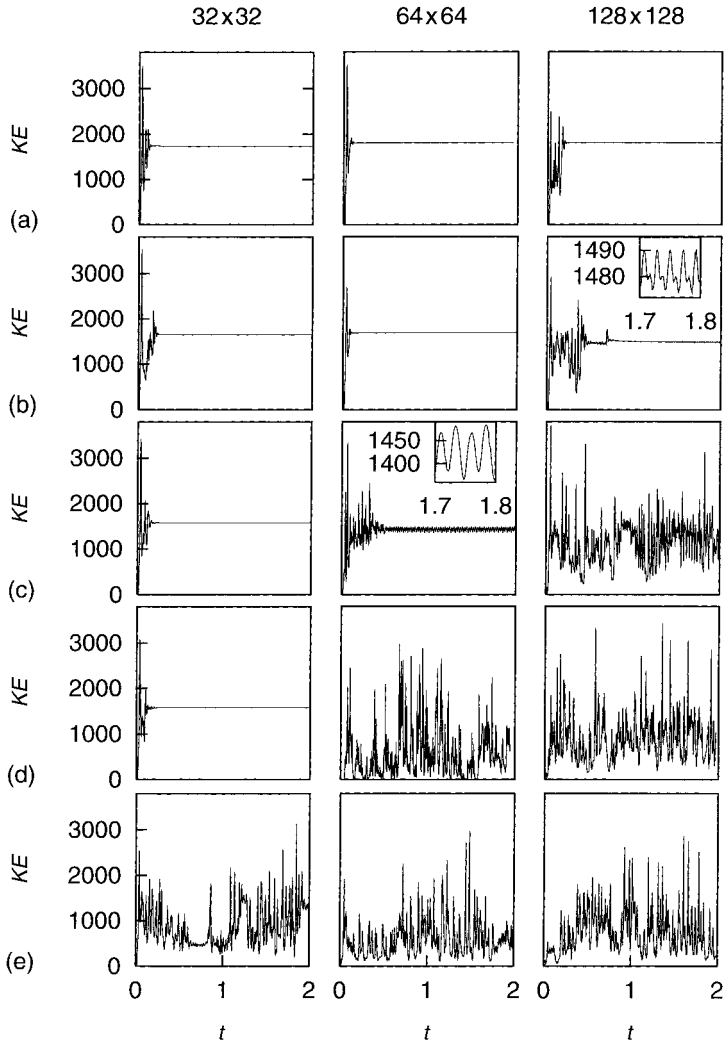

Figure 5. (a)–(e) Temporal evolution of *KE* for 15 simulations with various spatial resolution and for several buoyancy ratios: (a) $R_\rho = 0.2$, (b) $R_\rho = 0.3$, (c) $R_\rho = 0.4$, (d) $R_\rho = 0.5$, and (e) $R_\rho = 0.6$. Other parameters are similar to those in Figure 3. In two figures, the oscillatory character of the signal is elucidated by a closeup view.

balance between the most important forces, exerted on the interface, determines this transition. This force balance is used in the situation studied here, to check the stability of the interface shown in Figures 2(e)–(h).

In Figure 6, a schematic diagram is shown of the two convective layers and the intermediate density interface. The forces are defined per unit volume and are all divided by the factor μ/K (of which the value is defined implicitly with the Rayleigh number). This scaling is permitted as only the balance between the various forces is considered. The interface experiences three forces. First, the upward

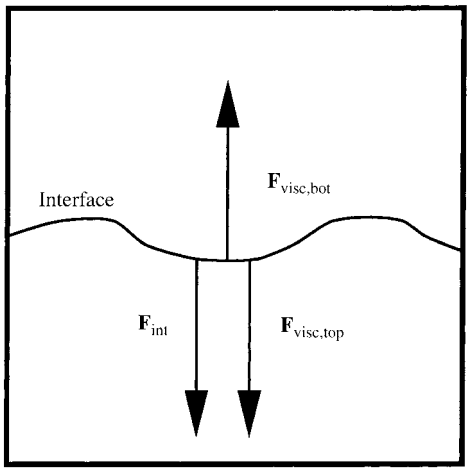

Figure 6. Schematic diagram of two convective layers separated by a density interface. The interface experiences three forces: a viscous drag force of the bottom convective layer $\mathbf{F}_{\text{visc,bot}}$, a viscous drag force of the top convective layer $\mathbf{F}_{\text{visc,top}}$, and a buoyancy force due to the density difference across the interface $\mathbf{F}_{\text{int}}$.

viscous drag force $\mathbf{F}_{\text{visc,bot}}$ in the bottom layer is defined as the buoyancy of a fluid parcel within this layer minus the pressure gradient over the parcel, divided by ϕ^*:

$$\mathbf{F}_{\text{visc,bot}} = \frac{\overline{\rho^* - (\partial p/\partial z)}}{\phi^*} = \frac{(q_z)_{\text{repr}}}{\phi^*}, \tag{7}$$

where Darcy's law has been used and $\rho^* = \text{Ra}_T(R_\rho C - T)$ is the difference between the buoyancy of the parcel and the buoyancy at the reference state. The factor ϕ^* is included in the force, because the solute advects upwards with the vertical pore velocity q_z/ϕ^* rather than with q_z. The subscript repr denotes that a representative value of the vertical velocity should be chosen as to represent the viscous drag force exerted on the interface. Obviously, the vertical velocity becomes negligible at the interface. Consequently, for a parcel just below the interface the viscous drag force $\mathbf{F}_{\text{visc,bot}}$ is nearly zero. This can be seen in Figure 7(a), in which the vertical profiles of both the absolute value of the lateral maximum of the vertical velocity and the horizontally averaged buoyancy ratio are plotted for the time instances corresponding with the snapshots in Figures 2(e)–(h). Since only the most vigorous plumes are able to scrape off the interface, the maximum value of the upward velocity in the lower layer (divided by ϕ^*) can be taken as to represent the viscous drag force exerted by the bottom convective layer:

$$\mathbf{F}_{\text{visc,bot}} = \frac{q_{z,\text{max,bot}}}{\phi^*}. \tag{8}$$

A similar choice of the viscous drag force has been proven to be successful for describing the limitation of the layer growth in simulations with $\phi^* = 0.1$ (Schoofs *et al.*, 2000).

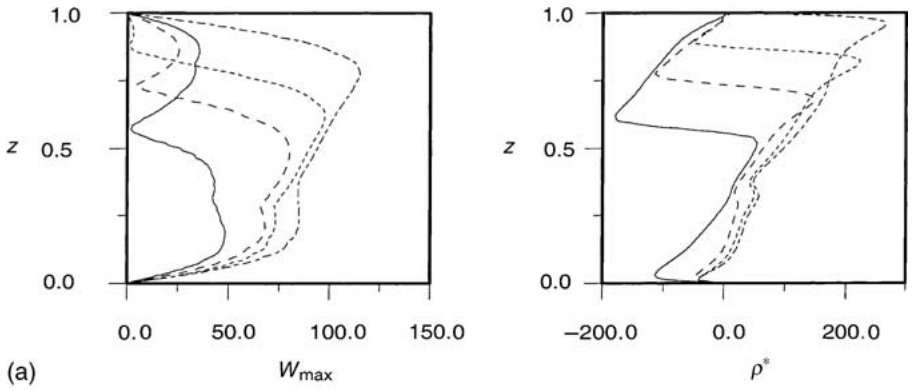

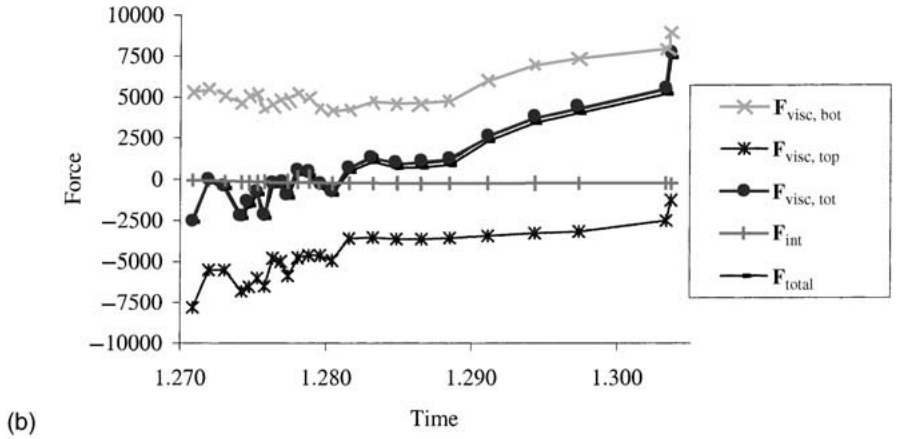

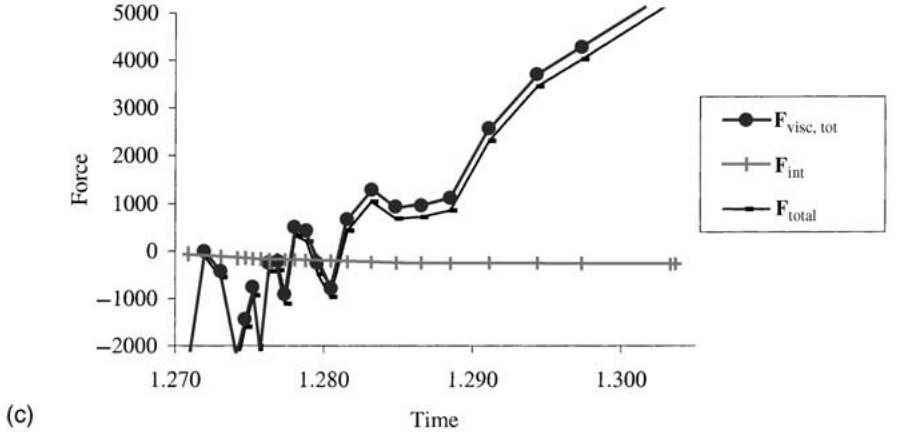

Figure 7. (a) Vertical profiles of the lateral maximum of the vertical velocity $q_{z,\max}$ and buoyancy ρ^* at similar time instants as those of the snapshots (e)–(h) in Figure 2. (b) The forces depicted in Figure 5, $\mathbf{F}_{visc,bot}$, $\mathbf{F}_{visc,top}$, $\mathbf{F}_{int}$, and the resulting forces $\mathbf{F}_{visc,tot}$, $\mathbf{F}_{total}$, plotted as a function of time. (c) Close-up view of (b), but only with $\mathbf{F}_{visc,tot}$, $\mathbf{F}_{int}$, and $\mathbf{F}_{total}$.

The second force, the downward directed viscous drag force in the upper layer, is defined in a similar way by

$$\mathbf{F}_{\mathrm{visc,top}} = \frac{q_{z,\mathrm{max,top}}}{\phi^*}. \tag{9}$$

The third force, finally, is exerted by the density interface itself and is also directed downwards:

$$\mathbf{F}_{\mathrm{int}} = \overline{\Delta\rho^*_{\mathrm{int}}} = \overline{\rho^*_{\mathrm{lower}} - \rho^*_{\mathrm{upper}}} \tag{10}$$

which is the horizontally averaged buoyancy difference across the interface.

The force balance states that convective entrainment across the interface (which leads to migration of the interface) occurs when the absolute value of the resultant of the two viscous drag forces, $|\mathbf{F}_{\mathrm{visc,tot}}| = |\mathbf{F}_{\mathrm{visc,bot}} + \mathbf{F}_{\mathrm{visc,top}}|$ is larger than the absolute interfacial buoyancy force $|\mathbf{F}_{\mathrm{int}}|$:

$$|\mathbf{F}_{\mathrm{visc,tot}}| > |\mathbf{F}_{\mathrm{int}}|. \tag{11}$$

The total force, $\mathbf{F}_{\mathrm{total}}$, is defined as the result of all forces

$$\mathbf{F}_{\mathrm{total}} = \mathbf{F}_{\mathrm{visc,bot}} + \mathbf{F}_{\mathrm{visc,top}} + \mathbf{F}_{\mathrm{int}}. \tag{12}$$

In order to validate the force balance, the forces are plotted as a function of time (Figures 7(b) and (c)) of an interface which exist between $t = 1.283$ and $t = 1.309$. The downward directed interfacial force $\mathbf{F}_{\mathrm{int}}$ gradually decreases with time from 0, at the start of the interface development, to a minimal value of -270 at $t \approx 1.305$. The absolute values of the viscous drag forces $\mathbf{F}_{\mathrm{visc,bot}}$ and $\mathbf{F}_{\mathrm{visc,top}}$ are not very accurate at the initial stages of the interface development, in which the interface is distorted. From the time instant that the interface has developed ($t \approx 1.285$), these forces are between 4×10^3 and 8×10^3; clearly much larger than the interfacial buoyancy force. The sum of the viscous drag forces, however, is of the same order of magnitude as the interfacial force: $\mathbf{F}_{\mathrm{visc,tot}}$ falls mostly between 0 and 1200 during this period (see Figure 7(c)). Still, the total viscous drag force becomes larger than the interfacial force. As predicted from the force balance (Eq. (8)), the interface is unstable from $t \approx 1.288$. Indeed, at that moment the interface starts to migrate upwards. The migration process is enhanced by the fact that the contrast in convective vigor between both layers increases, as can be seen by the fast growth of the total viscous drag force from $\mathbf{F}_{\mathrm{visc,tot}} \approx 1000$ at $t = 1.287$ to $\mathbf{F}_{\mathrm{visc,tot}} \approx 4000$ at $t = 1.297$.

From the results, it can be concluded that two conditions must be met for an interface to migrate upwards. First, the viscous drag force in the lower layer must be stronger than in the upper one. Secondly, the interfacial buoyancy force must be only slightly smaller than the viscous drag force in the lower layer. The convection currents in the lower layer can then entrain fluid across the interface, while the interface is strong enough to suppress deflections induced by the convection currents (Schoofs *et al.*, 2000). In case the interface force becomes very small, the

distorted interface will break down when it touches one of the boundary layers at the horizontal domain boundaries. For downward migration to occur, evidently, convection in the upper layer has to be stronger than in the lower layer.

7. Discussion and Conclusions

We have studied the stability and dynamics of TCC in a saturated porous medium with a porosity of 0.01 by means of numerical simulations of the set of full governing equations. Focus is both on the transition from steady to chaotic convection and on the flow dynamics in the chaotic regime for the case the fluid is heated and salted from below. It is shown that a transition from steady to chaotic flow occurs when the ratio between chemical and thermal buoyancy is increased, while the driving thermal buoyancy is kept constant. The transition is attributed to an increased influence of advective solute transfer over the more moderate convective heat transfer, the latter actually driving the flow. The observation of a limit cycle at the transition lead us to suggest, that the transition takes the form of a Hopf bifurcation. The critical buoyancy ratio depends slightly on the chosen spatial numerical resolution.

The flow pattern in the chaotic regime is characterized by irregular transitions between nonlayered and layered flow patterns. In the nonlayered mode, the flow pattern consists of several distinct areas, in which heat and solute transport is governed either by advection or by diffusion.

In the layered mode, gravitationally stable interfaces divide the domain into separately convecting layers of different solute concentration. Advective and dispersive entrainment across the interfaces results in upward or downward migration of the interfaces. The interface stability is analyzed in terms of a simple force balance. The interface is stable when the resultant of the maximum viscous drag forces in the two adjacent convective layers remains smaller than the buoyancy force exerted by the interface. For a typical example, the force balance describes the stability and migration of the interface very well.

The chaotic behavior of the flow evidently leads to an unsteadiness of the heat and solute transport across the domain. The dominant frequencies in the Nusselt numbers correspond with the frequency of the formation and disappearance of the interfaces. During the existence of an interface, heat and solute transport and the kinetic energy of the flow are all reduced considerably.

It would be interesting to investigate whether the transition from steady to chaotic convection via an increase in the buoyancy ratio, as found here in a two-dimensional square domain, does also take place at various aspect ratios and in three dimensions. It is known that the transition to chaos in three-dimensional experiments of pure thermally driven convection occurs at a lower thermal Rayleigh number as compared to two-dimensional experiments (Schubert and Strauss, 1979; Kimura *et al.*, 1989). A similar reduction of the critical R_ρ value may exist for the transition studied here.

We recognize that our model is only a simple representation of the complexities that arise in geological porous media. The permeability is assumed to be an isotropic scalar here, and the internal spatial scales of the porous medium are neglected. Furthermore, a simple mass balance and the applicability of Darcy's law is assumed, while a Fickian dispersion model is employed. All of these will probably affect the transition to chaos and the flow dynamics, but they are not within the scope of this study.

For typical geological parameters for a fractured domain (a domain height of 4 km, $\Delta T = 200$ K, and $K = 6 \times 10^{-14}$ m^2), chaotic convection occurs when the salinity contrast between top and bottom is approximately 5 wt% or more, at least for the two-dimensional flow studied here. Considering the large salinity gradients present within the crust, convection of aqueous fluids appears intrinsically unsteady within vast volumes of the Earth's crust.

Acknowledgements

Thanks goes to Ulrich Hansen and Ron Trompert for their close cooperation during parts of this work.

References

Alavyoon, F.: 1993, On natural convection in vertical porous enclosures due to prescribed fluxes of heat and mass at the vertical boundaries, *Intl. J. Heat Mass Transf.* **36**, 2479–2498.

Alavyoon, F., Masuda, Y. and Kimura, S.: 1994, On natural convection in vertical porous enclosures due to opposing fluxes of heat and mass prescribed at the vertical walls, *Intl. J. Heat Mass Transf.* **37**, 195–206.

Bear, J.: 1972, *The Dynamics of Fluids in Porous Media*, Dover Public., New York.

Cooper, C. A., Glass, R. J. and Tyler, S. W.: 1997, Experimental investigation of the stability boundary for double-diffusive finger convection in a Hele-Shaw cell, *Water Resour. Res.* **33**, 517–526.

Cooper, C. A., Glass, R. J. and Tyler, S. W.: 2001, Effect of buoyancy ratio on the development of double-diffusive finger convection in a Hele-Shaw cell, *Water Resour. Res.* **37**, 2323–2332.

Fisher, A. T.: 1998, Permeability within the basaltic oceanic crust, *Rev. Geophys.* **36**, 143–192.

Griffiths, R. W.: 1981, Layered double-diffusive convection in porous media, *J. Fluid Mech.* **102**, 221–248.

Hundsdorfer, W. and Trompert, R. A.: 1994, Method of lines and direct discretization: a comparison for linear advection, *Appl. Numer. Math.* **13**, 469–490.

Kimura, S., Schubert, G. and Straus, J. M.: 1986, Route to chaos in porous-medium thermal convection, *J. Fluid Mech.* **166**, 305–324.

Kimura, S., Schubert, G. and Straus, J. M.: 1989, Time-dependent convection in a fluid-saturated porous cube heated from below, *J. Fluid Mech.* **207**, 153–189.

Mamou, M., Vasseur, P. and Bilgen, E.: 1995, Multiple solutions for double-diffusive convection in a vertical porous enclosure, *Int. J. Heat Mass Transf.* **38**, 1787–1798.

Mamou, M., Vasseur, P. and Bilgen, E.: 1998, Double diffusive convection instability problem in a vertical porous enclosure, *J. Fluid Mech.* **368**, 263–289.

Mamou, M. and Vasseur, P.: 1999, Thermosolutal bifurcation phenomena in porous enclosures subject to vertical temperature and concentration gradients, *J. Fluid Mech.* **395**, 61–87.

Manning, C. E. and Ingebritsen, S. E.: 1999, Permeability of the continental crust: implications of geothermal data and metamorphic systems, *Rev. Geophys.* **37**, 127–150.

Murray B. T. and Chen C. F.: 1989, Double-diffusive convection in a porous medium, *J. Fluid Mech.* **201**, 147–166.

Nield, D. A.: 1968, Onset of thermohaline convection in a porous medium, *Water Resour. Res.* **4**, 553–560.

Nield, D. A. and Bejan, A.: 1999, *Convection in Porous Media*, Springer, New York.

Oldenburg, C. M. and Pruess, K.: 1998, Layered thermohaline convection in hypersaline geothermal systems, *Transport in Porous Media* **33**, 29–63.

Oldenburg, C. M. and Pruess, K.: 1999, Plume separation by transient thermohaline convection in porous media, *Geophys. Res. Lett.* **26**(19), 2997–3000.

Person, M., Raffensperger, J. P., Ge. S. and Garven, G.: 1996, Basin-scale hydrogeologic modeling, *Rev. Geophys.* **34**, 61–87.

Phillips, O. M.: 1991, *Flow and Reactions in Permeable Rocks*, Cambridge University Press, New York.

Rosenberg, N. D. and Spera, F. J.: 1992, Thermohaline convection in a porous medium heated from below, *Int. J. Heat Mass Transf.* **35**, 1261–1273.

Rudraiah, N., Shrimani, P. K. and Friedrich, R.: 1982, Finite amplitude convection in a two-component fluid saturated porous layer, *Int. J. Heat Mass Transf.* **25**, 715–722.

Schmitt, R. W.: 1994, Double diffusion in oceanography, *Annu. Rev. Fluid Mech.* **26**, 255–285.

Schoofs, S.: 1999, Thermochemical convection in porous media: an application to hydrothermal systems and magmatic intrusions, PhD Thesis, Geologica Ultraiectina, 179, Utrecht University, Utrecht.

Schoofs, S., Spera, F. J. and Hansen, U.: 1999, Chaotic thermohaline convection in low-porosity hydrothermal systems, *Earth Planet. Sci. Lett.* **174**, 213–229.

Schoofs, S., Trompert, R. A. and Hansen, U.: 1998, The formation and evolution of layered structures in porous media, *J. Geophys. Res.* **103**, 20843–20858.

Schoofs, S., Trompert, R. A. and Hansen, U.: 2000, The formation and evolution of layered structures in porous media: effects of porosity and mechanical dispersion, *Phys. Earth Planet. Int.* **118**, 205–225.

Schubert, G. and Straus, J. M.: 1979, Three-dimensional and multicellular steady and unsteady convection in fluid-saturated porous media at high Rayleigh numbers, *J. Fluid Mech.* **94**, 25–38.

Steen, P. H. and Aidun, C. K.: 1988, Time-periodic convection in porous media: transition mechanism, *J. Fluid Mech.* **196**, 263–290.

Trevisan, O. V. and Bejan, A.: 1987, Mass and heat transfer by high Rayleigh number convection in a porous medium heated from below, *Int. J. Heat Mass Transf.* **30**, 2341–2356.

Vadasz, P. and Olek, S.: 1999, Weak turbulence and chaos for low Prandtl number gravity driven convection in porous media, *Transport in Porous Media* **37**, 69–91.

Vadasz, P.: 1999, Local and global transitions to chaos and hysteresis in a porous layer heated from below, *Transport in Porous Media* **37**, 213–245.